Detection of Cracking Levels in Brittle Rocks by Parametric Analysis of the Acoustic Emission Signals

Citation: Moradian, Zabihallah, Herbert H. Einstein, and Gerard Ballivy. “Detection of Cracking Levels in Brittle Rocks by Parametric Analysis of the Acoustic Emission Signals.” Rock Mechanics and Rock Engineering 49, no. 3 (June 16, 2015): 785–800.

Published Version: http://dx.doi.org/10.1007/s00603-015-0775-1

Publisher: Springer-Verlag

Permanent Link: http://hdl.handle.net/1721.1/101879

Version: Author's final manuscript: final author’s manuscript post peer review, without publisher’s formatting or copy editing

Detection of cracking levels in brittle rocks by parametric analysis of the acoustic emission signals

Zabihallah Moradian[*1, 2], Herbert H. Einstein[1], Gerard Ballivy[2]

1. Massachusetts Institute of Technology (MIT), Department of Civil and Environmental Engineering, 77 Massachusetts Avenue, Cambridge, MA, 02139
2. Department of Civil Engineering, Université de Sherbrooke, 2500 Boulv. de L'université, Sherbrooke, Qc, Canada J1K2R1

Abstract

Determination of the cracking levels during the crack propagation is one of the key challenges in the field of fracture mechanics of rocks. Acoustic emission (AE) is a technique that has been used to detect cracks as they occur across the specimen. Parametric analysis of AE signals and correlating these parameters (e.g. hits and energy) to stress-strain plots of rocks let us detect cracking levels, properly. The number of AE hits is related to the number of cracks, and the AE energy is related to magnitude of the cracking event. For a full understanding of the fracture process in brittle rocks, prismatic specimens of granite containing pre-existing flaws have been tested in uniaxial compression tests, and their cracking process was monitored with both AE and high-speed video imaging. In this paper the characteristics of the AE parameters and the evolution of cracking sequences are analyzed for every cracking level. Based on micro- and macro-crack damage, a classification of cracking levels is introduced. This classification contains eight stages 1) crack closure, 2) linear elastic deformation, 3) micro-crack initiation (white patch initiation), 4) micro-crack growth (stable crack growth), 5) micro-crack coalescence (macro-crack initiation), 6) macro-crack growth (unstable crack growth), 7) macro-crack coalescence and 8) failure.

Keywords: Brittle rocks, fracture mechanics, flaw, cracking levels, acoustic emission, AE hits, AE energy

1. Introduction

Understanding the cracking levels such as crack initiation, crack propagation and crack coalescence in rocks allows us to have a better understanding of the rock behavior. This information will eventually provide good input data for numerical analyses of geotechnical engineering projects. Thus it is important to establish the thresholds associated with micro-scale and macro-scale cracking (Brace 1964, Bieniawski 1967a, Wawersik and Fairhurst. 1970).

Various methods have been proposed to identify cracking levels by using laboratory test results and numerical simulations. Researchers have tried to divide the stress-strain plots of rocks, tested in uniaxial and triaxial laboratory experiments, into critical stages so called cracking levels. Based on the stress-strain behavior of rocks Brace (1964) and Bieniawski (1967a) defined these stages as (1) crack closure, (2) linear elastic deformation, (3) crack initiation and stable crack growth, (4) critical energy release and unstable crack growth, and (5) failure and post-peak behavior. The most common methods that researchers have used to detect the cracking levels during laboratory compression loading involves the use of electric resistance strain gauges to

[*] Corresponding author

E-mail address: moradian@mit.edu, Tel: 1 617 258 8070 (Zabihallah Moradian)

measure slight changes in specimen deformation that can be related to the closing and opening of cracks (Eberhardt et al. 1998).

Researchers have suggested that the crack initiation observed in laboratory compression tests provides a good estimate of the operational spalling strength observed in hard brittle rocks around underground openings (Diederichs, 2007; Andersson et al., 2009; Martin and Christiansson, 2009; Rojat et al., 2009). Damjanac and Fairhurst (2010) suggested that crack initiation may also be used as a lower bound estimate for the long-term strength threshold of crystalline rocks. Other researchers suggest that crack initiation related to the Kaiser effect (will be discussed later) can be used to establish the in-situ state of stress (Seto et al. 1999). Nicksiar and Martin (2012) proposed that the ISRM (International Society for Rock Mechanics) suggested methods be revised to include procedures suitable for establishing the crack-initiation stress.

The methods for detecting crack initiation have utilized either the volumetric strain or the lateral strain (Brace et al, 1966; Bieniawski, 1967b; Lajtai, 1974; Stacey, 1981), and have been modified by various researchers (Martin and Chandler, 1994; Diederichs, 2007, Nicksiar and Martin 2012).

It has been shown that crack initiation is difficult to identify from the volumetric strain method, particularly if the specimen already contains a high density of cracks. On the other hand, analysis of the laboratory tests revealed that the lateral strain versus axial strain is nonlinear and therefore applying this approach is problematic (Andersson et al. 2009, Nicksiar and Martin, 2012). As a result a certain degree of subjectivity may be introduced by picking the cracking levels using lateral and volumetric strain curves.

Other techniques involve the use of photoelastics, optical diffraction patterns, scanning electron microscopy, laser speckle interferometry, ultrasonic probing, and electrical resistivity and AE techniques (Eberhardt et al. 1998, Diederichs et al. 2004).

Following Griffith (1921), it has been widely accepted that the failure process of brittle rocks is controlled by pre-existing flaws. As a result, several studies have been done by the MIT rock mechanics group for detecting crack initiation, -propagation and -coalescence of brittle rocks containing pre-existing flaws. In these studies, the determination of cracking levels and types (shear/tensile) was based on the identification of fractographical features and on high-speed images of the cracks (Bobet and Einstein 1998, Miller and Einstein 2008, Wong and Einstein 2009a and 2009b). They found crack initiation in the form of white patches around the flaw tips. Using environmental scanning electron microscopy (ESEM) and photographical monitoring of images, they qualitatively related this white patching to the development of micro-cracks. Obviously, this approach is limited. The front surface of each specimen is the only part observed directly. Hairline cracks on the front face may be through-going or they may just be on the surface (Miller 2008).

AE can be used to detect and locate cracks as they occur, across the entire specimen. By using AE analysis, crack initiation within the specimen (surface or volume) can be investigated. By comparing the results of the AE with high speed camera images, the time between a crack developing and a visible crack propagating can be found, as well as the energy involved in cracking and the size of the fracture process zone.

Correlating parameters of the detected AE signals with a growing crack is considered to be a very good tool to investigate cracking sequences of materials under stress. AE parametric features are extracted and provide good information about the failure behavior of materials, and they help to estimate the evolution of cracking process. AE techniques have been used widely in rock mechanics, but up to now, they were not much used to explore the initiation, propagation

and coalescence of brittle rock containing fissures. Eberhardt et al. 1998 tried to determine crack initiation stress thresholds of intact rocks by using a moving point regression technique to the stress-strain data and an examination of the changes in the acoustic event properties with loading. However, the insignificant AE activity in the crack initiation stages made it difficult to differentiate between the background noise and the cracking-source acoustic events (Nicksiar and Martin 2012).

The objective of this paper is to demonstrate AE as a technique for detecting cracking levels in rocks. To this end, prismatic specimens of granite containing pre-existing flaws were tested under uniaxial compressive loading. By correlating AE parameters with the stress-strain response of the tested rocks, cracking levels can be identified, especially micro-cracking and macro-cracking.

2. Experimental Procedure

Samples tested in this research are Barre granite specimens that were cut from blocks of a quarry in Vermont (Adam's Granite Company Inc.). Barre granite's mineral content typically consists of approximately 36% plagioclase, 32% quartz, 18% K-feldspar, 8% biotite, 3% muscovite, and 3% granophyres minerals (Goldsmith et al. 1976). It is a fine to medium grained rock with mineral grain sizes ranging from 0.25 to 3 mm (Xia et al. 2007). The material properties of Barre granite are presented in Table 1.

The prismatic specimens (6 × 3 × 1 in; ~152mm ×~76mm×~25mm) were usually cut with a diamond saw. The pre-existing flaws (length 2a=0.5" (~13 mm), where a is the flaw half length) were always cut into the specimen using an OMAX water jet. The flaw pairs are defined by flaw inclination angles (β), bridging angles (α) and ligament lengths (L) (Figure 1). A geometry of 2a-30-30 means that it has ligament length=0.5"(~13 mm), flaw incliniation angle=30^0 and bridging angle =30^0.

A total of 11 granite specimens were tested for this study. Figure 2 displays a granite specimen with the position of the attached AE sensors.

Table 1: Rock mechanics properties of the Barre granite specimens

Young's Modulus (GPa)	19.2 (Miller (2008))
Compressive Strength (MPa)	151 (Miller (2008))
Tensile Strength (MPa)	5.08-10.65 (Goldsmith et al. (1976))
P-wave velocity (m/s)	4000

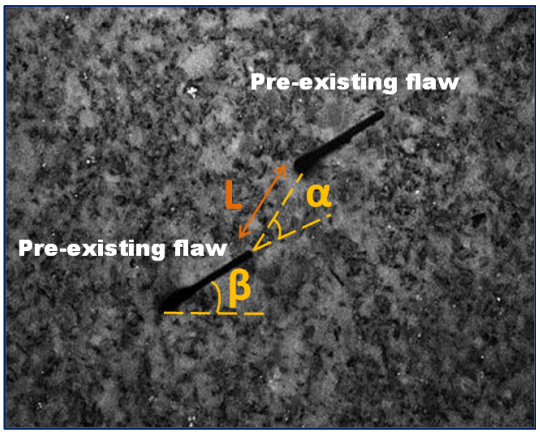

Figure 1: Schematic of the pre-existing flaws with β the flaw inclination angle, α the bridging angle and L the ligament length.

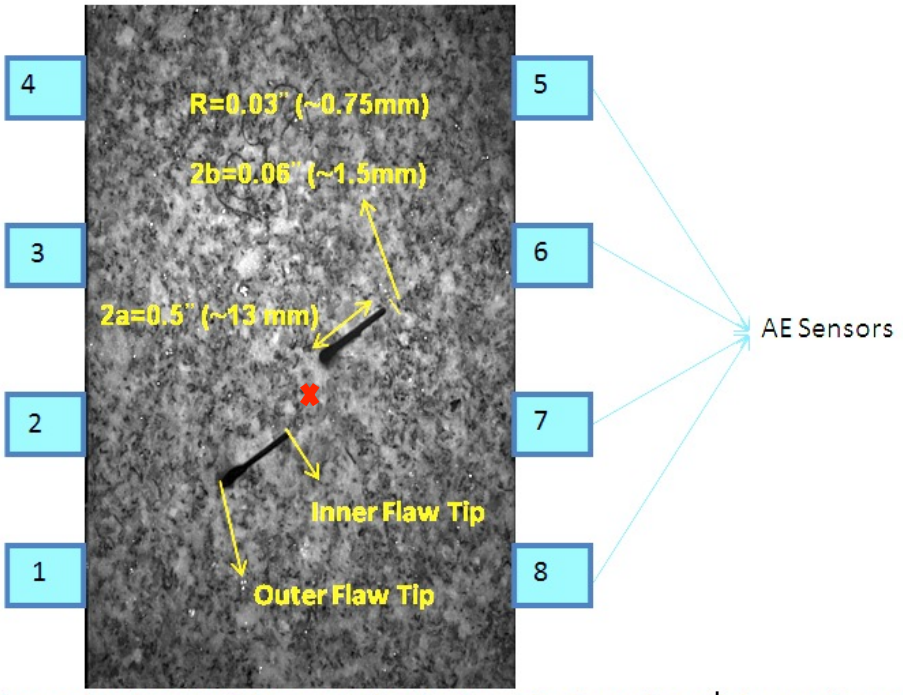

Figure 2: Prismatic granite specimen tested under uniaxial compression loading. The dimensions of the specimen are 6" (~152 mm)* 3" (~76 mm)* 1"(~25 mm). The flaws have a length of 0.5"(~13mm) and rounded tips with inner curvature radius of 0.03" (~0.75mm). Eight sensors were attached to sides of the specimen. The sensors are numbered from 1-8 starting clockwise from the bottom left.

The specimens were uniaxially loaded in a 200-KIP BaldwinTM hydraulic loading frame. The data were collected with a program called MTestW, which records the load, displacement and time electronically. Each specimen was loaded at a slow initial rate to eliminate seating effects (0.0017 in/s (~ 0.4318 mm/s) to 1000 lb (~ 4448 N), then 0.003 in/s (~ 0.762 mm/s) to 2500 lb (~ 11120 N), after which loading continued at a constant rate, 38.34 lb/s (~ 170.54 N/s), until failure or the manual stopping of the test (Brooks et al. 2013).

High speed imagery was captured using a Phantom TM V-series high speed camera controlled by a separate laptop computer. This high-speed camera captures approximately 5404 images in 1.081 sec at 512×512 pixel resolution. The high-speed camera was electronically connected to the loading frame, which detected failure by a significant drop in load and thus triggered the high-speed capture. The test was also videotaped in real time with a SonyTM Camcorder. Steel brush platens were used on the specimen boundaries to reduce end effects. A photograph of the test setup is shown in Figure 3. Figure 4 displays the photo of a granite specimen (AE-GR-2a-30-30) before and after the test.

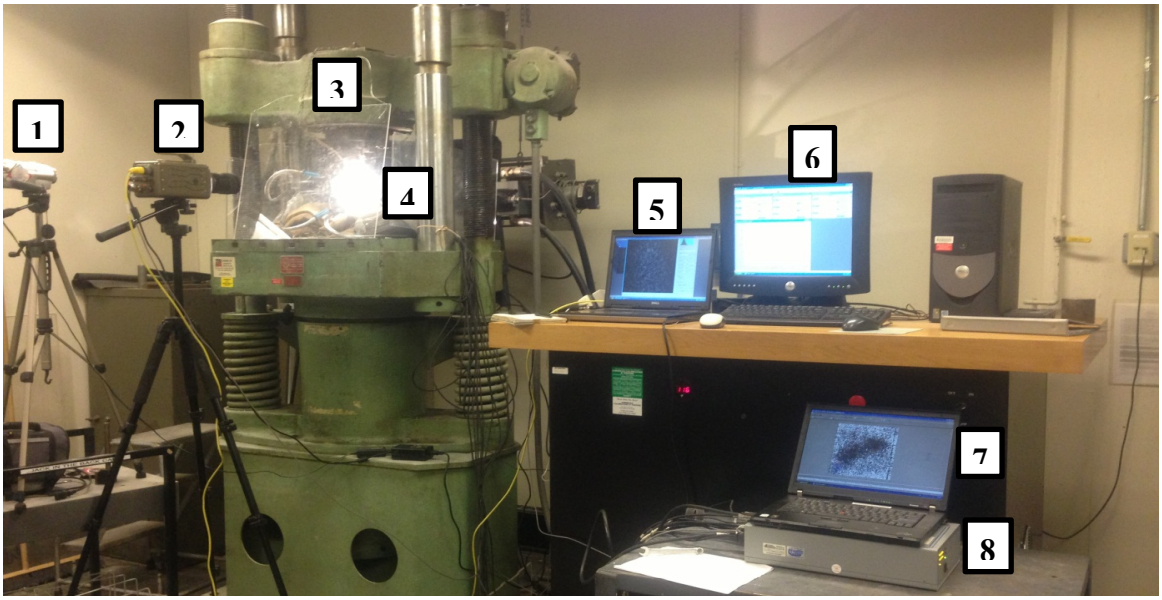

Figure 3: Photo of the test set up. 1) Sony Camcorder, 2) HSV (high speed video) Camera, 3) Baldwin Loading Frame, 4) Granite Specimen, 5) HSV (high speed video) Laptop, 6) MTestW Control, 7) AE Laptop and 8) AE Acquisition System.

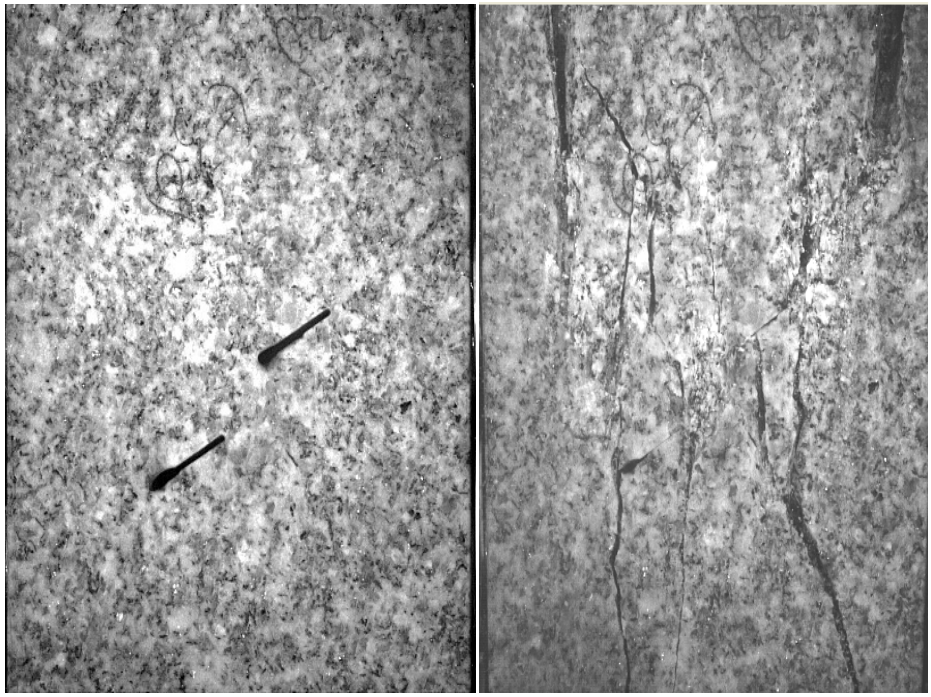

Figure 4: Photo of the AE-GR-2a-30-30 specimen before and after the test

3. AE Signal Detection

3.1. AE Signal Path

The path that an AE signal takes from the source to the PC monitor consists of: material, material boundary, coupling, sensor, cable, pre-amplifier and data acquisition (DAQ) system. Along this path some phenomena such as attenuation, reflection, refraction and mode conversion change the shape and the properties of the original signal. Although Barre granite is homogeneous and isotropic and the distance between sensors and the source in the tested specimens is short (maximum 150 mm), it is believed that still some changes may happen in the shape of the AE signals while they pass through the material. The small size of the specimen and its prismatic shape may cause signal reflection so that the resulting detected signal will be a superposition of the directly propagating signal from the source, along with all reflections. Depending on the size and complexity of the geometry, the superposition of these signals can produce a resultant waveform that is different from that caused by the original source. The reflection phenomenon is almost inevitable for all AE laboratory tests. That's why for source mechanism using AE testing, the focus is mostly on the arrival parts of the signals rather than the whole signal.

Another important factor affecting the shape of the detected signals is the type and the thickness of the coupling used between sensors and the surface of the specimen. For minimizing the effect of coupling on the AE signals a thin adhesive superglue was used to attach the sensors perfectly to the specimens. Nevertheless, the efficiency of the coupling was verified by pencil lead break (PLB) and auto sensor testing (AST).

Figure 5 shows waveforms and fast Fourier transforms (FFTs) of a microseismic event located between flaws (red star in Figure 2) and detected by all sensors. This Figure demonstrates how a single source may be detected differently by sensors located in different places. This is due to the

aforementioned phenomena occurring for the signal through its path (attenuation, reflection, mode conversion, effect of coupling etc.).

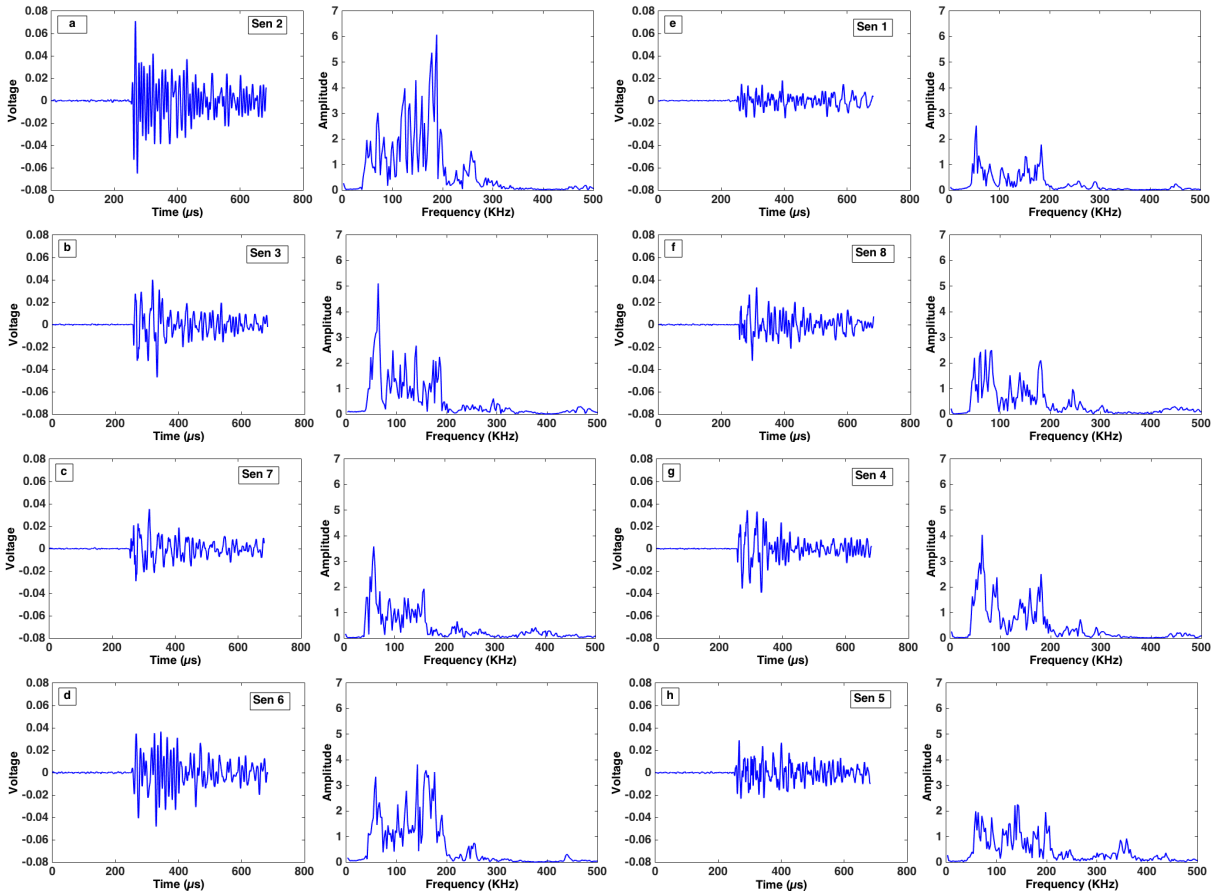

Figure 5: Waveforms and FFTs of an event located between flaws (red star in Figure 2) detected by all eight sensors. Based on threshold passing arrival time, sensors 2, 3, 7, 6, 1, 8, 4 and 5 have detected the event respectively (closer sensor detects the signal earlier). Since the path from the source to the sensors is different for each sensor, the detected waveforms are different. The existence of the flaw in the path of the generated signal to the sensors 1 and 5 causes higher amount of attenuation.

With regards to low frequencies, below 20 KHz, ambient noises interfere with measurement of signals with low amplitudes. For high frequency signals, attenuation problems are encountered since they decay much faster. In the current setup resonant sensors, R6I-AST integral preamplifier from Physical Acoustic Cooperation (PAC), with operating frequency range of 40-100 kHz and resonant frequency of 55 kHz were used.

The pre-amplifier is required since the voltages from the sensors are low and would acquire too much noise if the signal is sent directly to the DAQ. The boost from the pre-amplifier is expressed similarly to sensor sensitivity as dB=20logG, where G is the gain factor. A common amplification of 40dB was used which corresponds to $10^{\frac{40}{20}} = 100$ times. Thus, signal conditioning at or near the sensor is necessary to allow transmission to and detection by the DAQ system. For this purpose, low noise preamplifiers are usually placed at a cable distance of no more than 1.2m from the sensors. In this study, PAC 2/4/6 preamplifiers with 20 dB, 40 dB and 60 dB gain ranges were used.

The two common DAQ setups are continuous-based streaming (for continuous signals) and hit-based streaming (for burst signals). In the continuous streaming method, the system registers everything and therefore consumes significant memory space. As a result, the analysis can become more difficult due to extreme volume of data. The user then defines the hits from the continuous data file and calculates the parameters. Since rock fractures produce burst type signals, hit-based method is used mostly. In this method, the system saves as much information as is reasonably required, and therefore the technique is cheaper in cost and in storage space. The user must define the threshold in which a balance must be struck between setting signal threshold limits high enough to filter out the majority of the background noises, yet low enough to pick up the beginning of the microfracturing process (Eberhardt et al. 1998), though there are certain mechanical and hydraulic noises which have broad spectral content like cracking related acoustic emission events.

The DAQ system was a μSAMOS with 16 channels. The AEwin software with hit-based mode was used for acquisition of the AE parameters and registering the waveforms. AE hardware was set up with a threshold of 35 db, preamplification of 40, sampling rate of 3 MSPS, sample length of 3K and a band-pass filtration of 20-400 KHz.

When arrival signal passes the threshold, the sensor detects it and the exact time of arrival in test time is recorded. When the signal amplitude reaches a maximum and starts to decline, the DAQ card notes the maximum amplitude, and waits an additional peak definition time (PDT) to see if the previous signal amplitude is exceeded (Figure 6). If it is, the measurement continues. If there is no higher amplitude signal within the PDT, the previous amplitude is defined as the peak amplitude. As the signal continues, the card always records the time of the last threshold crossing. If there is no further crossing within the hit definition time (HDT), the last recorded time defines the end of the signal. If signal never goes under the threshold within the HDT, the system continues registration of the waveform until a certain time period (Max duration) and then it automatically defines the end of the signal.

After either HDT or Max Duration has been reached, the DAQ card waits until the HLT (hit lockout time) expires. At this point, the DAQ card is reset and ready to acquire the next signal. The HLT time prevents the channel from treating a reflection of the first signal as a new emission. However, an excessively long HLT time can prevent the capture of rapidly occurring emissions. Simultaneously with these time measurements, the card is also digitizing the signal and storing it, in case waveforms are desired. In this study by considering all of mentioned issues, PDT, HDT and HLT were set as 300, 800 and 1000 μsec. Different max duration setups were considered that will be discussed later.

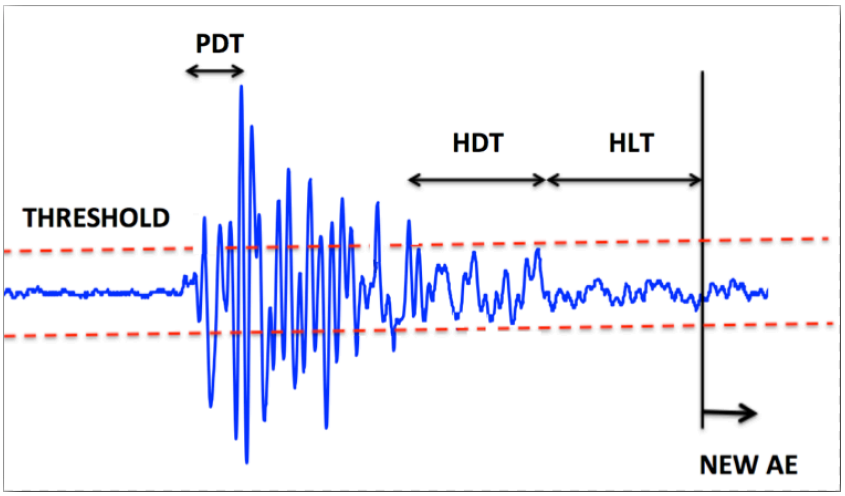

Figure 6: PDT, HDT and HLT for hit-based data registration method

Each cracking produces an AE event. Every sensor individually detects the AE event as an AE hit. In this study the maximum number of hits corresponding to an AE event can be 8 which is related to the number of used sensors.

3.2. AE Parameters

In addition to recording the number of acoustic hits and correlating this number to the measured deformation response in the rock, it is also possible to record certain properties of the AE waveforms. Common parametric features of the waveforms employed for evaluating AE characteristics are hits, amplitude, counts, duration, energy and rise time. Frequency domain features such as peak frequency and frequency centroid are also determined from the fast Fourier transform FFT of the recorded waveforms. Figures 7 and 8 show the common AE features in the time and frequency domains. Table 2 lists the AE parameters of the waveforms displayed in Figure 5. It can be seen in Table 2 that same event may produce different hits in the sensors depending on the path that the source signal takes from the event source to the sensor.

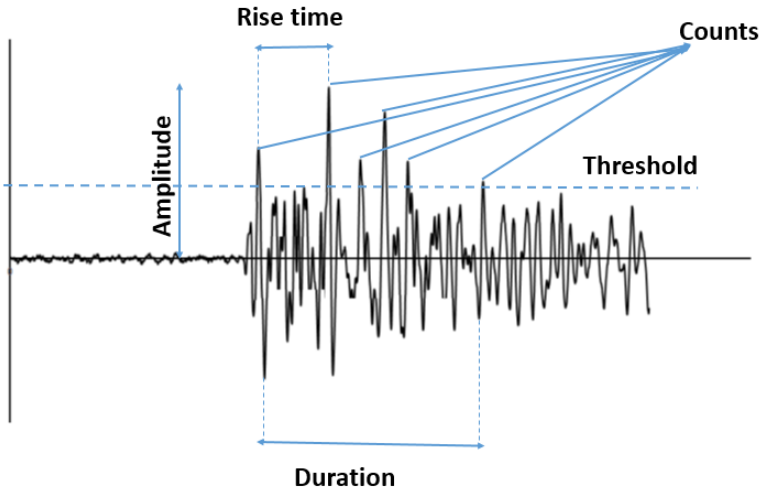

Figure 7: Common parameters of an AE waveform in time domain. Amplitude is the highest peak voltage of the signal, counts are the number of the times that the signal crosses the threshold, duration is the time interval between the first and the last threshold crossing, rise time is the time interval between first threshold crossing and the signal peak and energy is the area under the envelope of the signal.

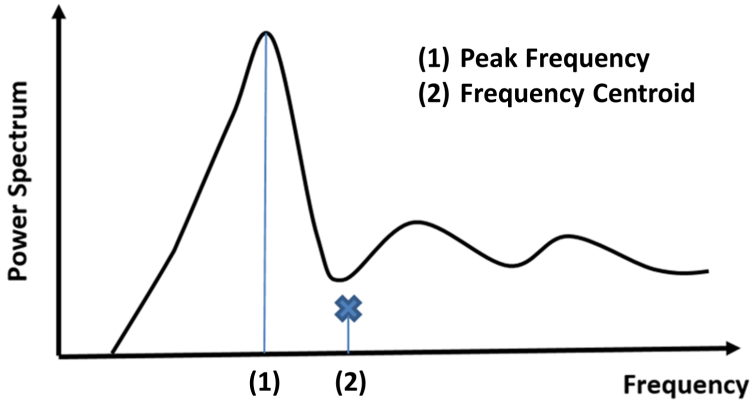

Figure 8: Peak frequency is the point where the power spectrum is greatest and frequency centroid is the center of mass of the power spectrum graph.

Table 2: AE parameters of the waveforms displayed in Figure 5

Threshold passing arrival time (s)	Channels (ordered based on arrival time)	Rise time (µs)	Counts	Energy (10µvolt-sec/count)	Duration (µs)	Amplitude (db)	Threshold (db)	Frequency centroid (KHz)	Peak frequency (KHz)
127.4253255	2	74	30	7	891	53	35	140	82
127. 4253265	3	59	29	6	1005	51	35	154	26
127. 4253275	7	74	30	7	1011	52	35	156	35
127. 4253280	6	54	33	6	952	50	35	155	41
127. 4253315	1	9	76	14	1495	57	35	125	111
127. 4253360	8	9	44	7	1159	49	35	162	84
127. 4253390	4	71	57	11	1177	54	35	123	32
127. 4253398	5	136	24	4	827	45	35	172	29

Considering all of mentioned problems, one may think of AE as a technique that suffers from many obstacles. It's true, when the AE results need to be analyzed quantitatively. In other words, if a quantitative analysis is done on the AE results, all of the mentioned problems must be taken into account. But if a qualitative analysis such as monitoring cracking trend or cracking sequences is required, even with distorted signals due to attenuation, reflection and so on, one may get interesting results, specifically if the results are double checked with another technique. In this paper, the efficiency of the AE results will be verified by high speed camera images.

4. Classification of Cracking Levels

The number of AE hits is proportional to the number of growing cracks, and the energy of the AE signals is proportional to the magnitude of cracking event in materials (Lockner 1993).
Figures 9 shows the rate and cumulative plots of the AE hits of the detected signals versus the applied uniaxial stress normalized by the peak strength. As will be shown and discussed in this section, different cracking levels can be observed by parametric analysis of the AE signals. These levels are:

1) Crack closure
2) Linear elastic deformation
3) Micro-crack initiation (white patch initiation)
4) Micro-crack growth (stable crack growth)
5) Micro-crack coalescence (macro-crack initiation)
6) Macro-crack growth (unstable crack growth)
7) Macro-crack coalescence
8) Failure.

Figure 10 depicts these cracks levels in the stress-strain plot.

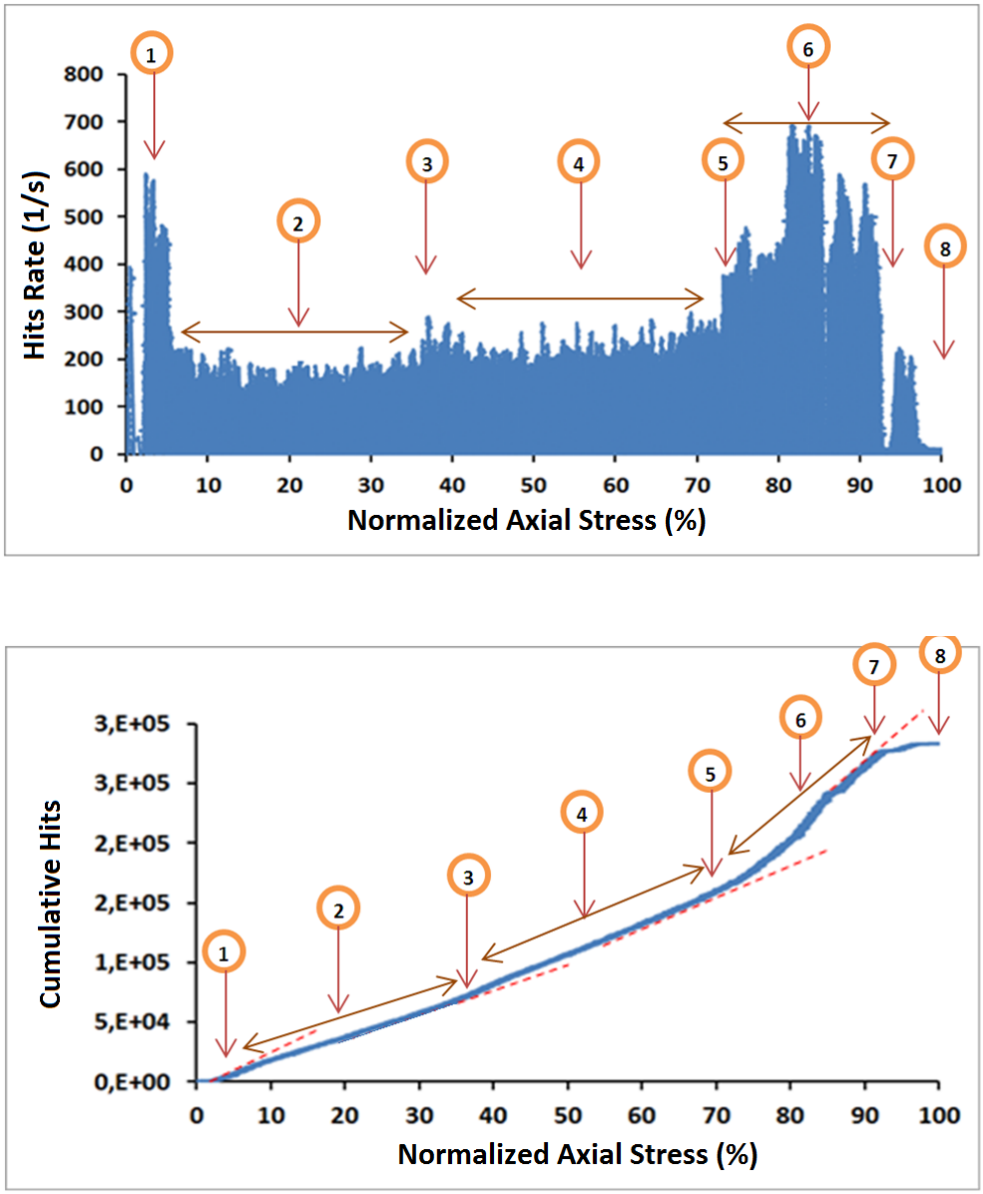

Figure 9: Plots of a) AE hits rate (per second) and b) cumulative AE hits versus the applied uniaxial stress normalized by the peak strength for the granite specimen AE-GR-2a-30-30.1) Crack closure, 2) linear elastic deformation, 3) micro-crack initiation (white patch initiation), 4) micro-crack growth (stable crack growth), 5) micro-crack coalescence (macro-crack initiation), 6) macro-crack growth (unstable crack growth), 7) macro-crack coalescence and 8) failure.

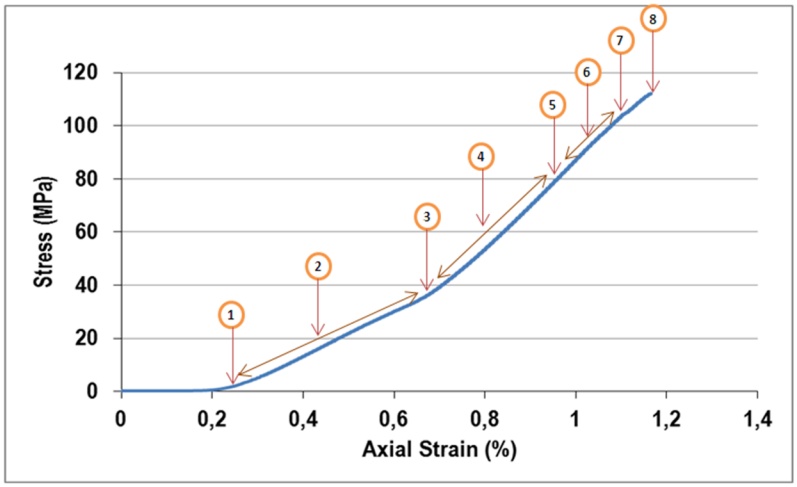

Figure 10: Axial stress (MPa) vs. axial strain (%) and cracking levels for the granite specimen AE-GR-2a-30-30. 1) Crack closure, 2) linear elastic deformation, 3) micro-crack initiation (white patch initiation), 4) micro-crack growth (stable crack growth), 5) micro-crack coalescence (macro-crack initiation), 6) macro-crack growth (unstable crack growth), 7) macro-crack coalescence and 8) failure.

In order to further study the cracking process in granite specimens, photographic monitoring was adopted during the uniaxial compression tests. On the basis of the photographic monitoring results, the real-time cracking sequences of specimens were identified and characterized. For every loading increment, a photo of the specimen was taken and by putting a trigger in the high-speed camera the moment of failure was filmed. Moreover, the corresponding axial stress and strain of cracking levels in the specimens were also obtained. Figure 11 displays the photographs of the sample for each cracking level.
In the following, the stress-strain curves, AE parametric analysis and photographical monitoring with high speed camera images are used to interpret what is happening during every cracking level.

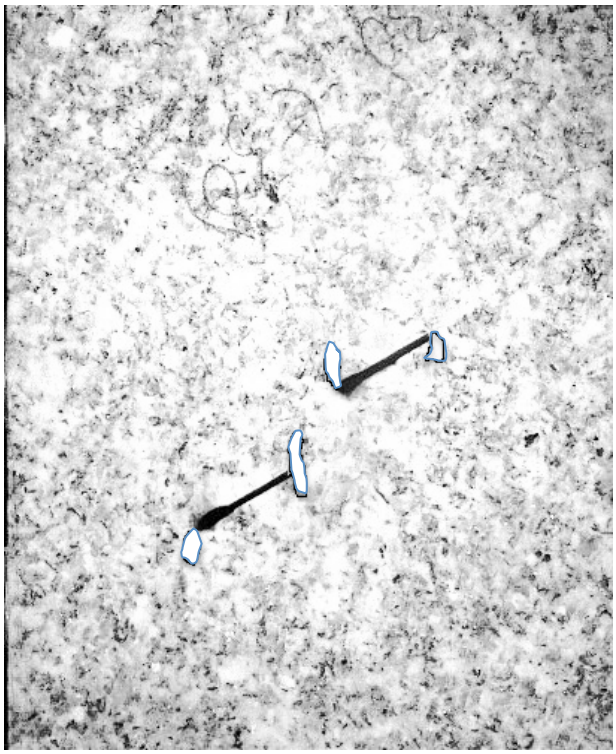

a: Micro-crack initiation (40% maximum loading, 42 MPa, 0.65 % axial strain). Micro-cracks show off as the form of white patches.

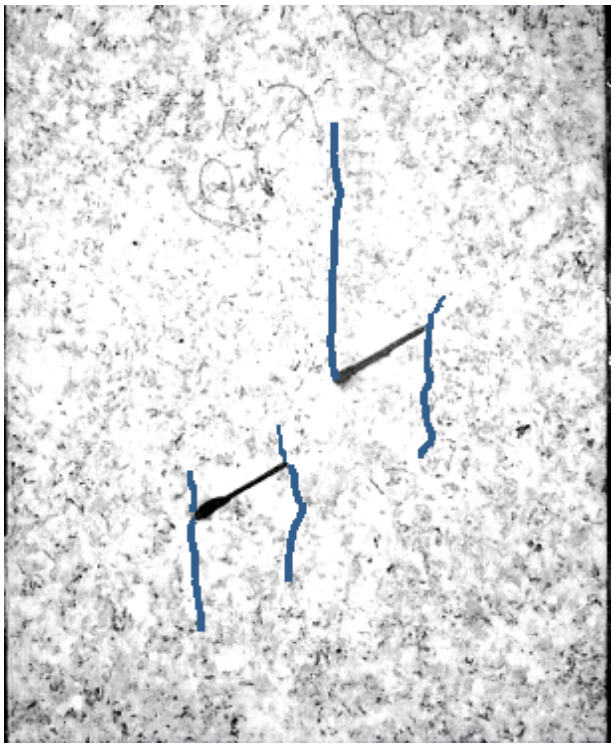

b) Macro-crack initiation (74% maximum loading, 81 MPa, 0.95 % axial strain).

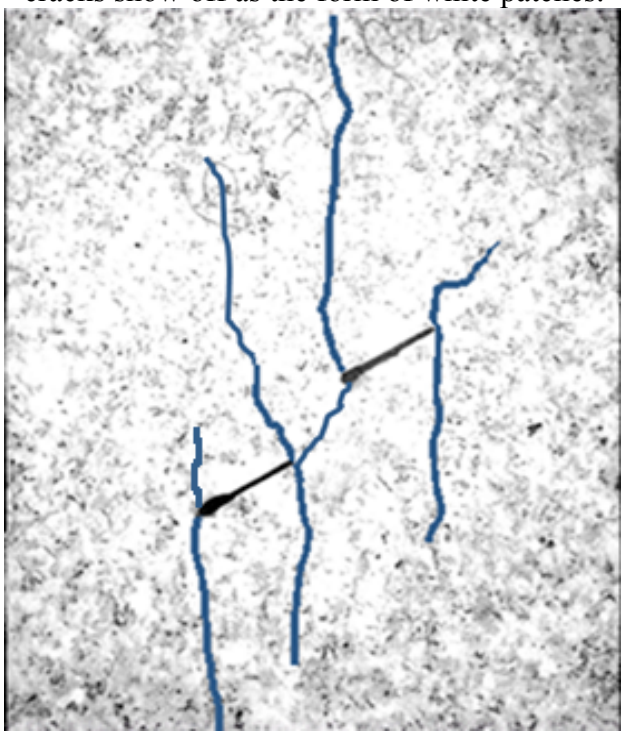

c) Macro-crack coalescence (92% maximum loading 102 MPa, 1.1 % axial strain).

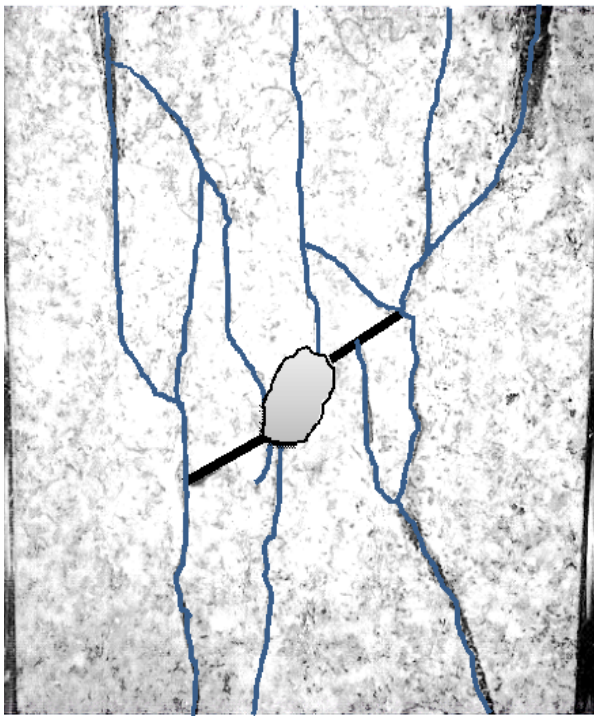

d) Failure (110 MPa, 1.2 % axial strain). Spalling occurred between two inner flaw tips.

Figure 11: Photos of the granite specimen AE-GR-2a-30-30

4.1.Crack Closure

The stress-strain graph is the best tool for observing this cracking level. Crack closure occurs during the first stages of loading when pre-existing cracks oriented at an angle to the applied load close. During crack closure, the stress-strain graph is nonlinear, displaying an increase in axial stiffness (level 1 in Figure 10). The extent of this nonlinear section depends on the crack density and geometrical characteristics of the crack population (Eberhardt et al. 1998). AE parameters show some activity in this part (stage 1 in Figure 9a). It should also be noted that some of this AE activity comes from the loading rate changes in this part. At the end of this stage the initial increase in acoustic emissions (related to crack closure and other system effects) gradually drops off. Checking the high speed camera photos did not reveal any significant information about this stage.

4.2.Linear Elastic Deformation

Once the majority of pre-existing cracks have closed, linear elastic deformation takes place in the stress-strain graph (level 2 in Figure 10). In this part, AE signals show constant-magnitude AE activity (stage 2 in Figure 9a). From Figure 9b, it can be seen that the slope of the cumulative AE graphs is linear in stage 2, indicating a constant AE activity. Again in this stage, the high speed camera photos did not reveal any significant information.

Eberhardt et al. (1998) stated that during the elastic deformation period, the lateral stiffness begins to decrease; possibly signifying shear or sliding movement between the faces of closing or closed cracks. This behavior has been observed in glass plates by Bieniawski (1967b) who noted that the sliding deformation demonstrated by single closed cracks continues even during linear elastic behavior.

4.3.Micro-Crack Initiation (White Patch Initiation)

At Level 3 in Figure 9a the acoustic emissions are different as an increase in AE hits occurs at 30-40% of peak strength. This behavior has been detected in almost all granite samples tested in this study.

In order to fully understand this change, the AE energy of the signals was measured. Plots of the AE energy and its stress-dependent rate change (Figure 12) show that the AE energy does not, or only slightly increase after level 3. It could be said that at level 3 a large number of small cracks (corresponding to high number of AE hits in Figure 9a) begin to grow, however, because of their low AE energy, they have very little effect in decreasing the overall competency of the rock.

Checking high speed camera photos (Figure 11a) revealed that some white patches appeared near or at the tips of the flaws parallel to the axial loading direction. Other researchers from the MIT rock mechanics group (Wong and Einstein 2009a and 2009b, Morgan et al. 2013 and Brooks et al 2013) have been able to interpret these white patches as zones of micro-cracks based on SEM investigations.

White patches were detected at around 40% peak strength, which is somewhat later than what was detected by AE parameters (around 35%). This may be due to the heterogeneous nature of granite's mineral composition that makes it difficult to identify micro-crack initiation using photographic monitoring. Another possibility for this delay is that high speed camera photos were taken from the surface of the specimen, while micro-cracking may start from inside. This means that micro-cracks have already been initiated, and that it takes a while to be detected by high speed camera imaginary, whereas with AE they are detected right after initiation.

Among cracking levels, this level has been investigated by many researchers. They have simply called it as 'crack initiation' without any differentiation between micro and macro-cracks. The early work of Brace et al. (1966) showed that the crack initiation for granite, marble and aplite occurred between 0.3 and 0.7 of the peak strength. More recently, Nicksiar and Martin (2013) showed that crack initiation was observed in all 376 specimens of low porosity rocks tested in compression. They showed that the ratio of crack initiation stress to uniaxial compressive strength remained well constrained at approximately 0.45 ± 0.06.

Cracking level 3 detected by AE monitoring (Figure 9) is in good agreement with the findings of these studies confirming it as crack initiation point. On the other hand, this point coincides with white patch initiation in photographical monitoring of high speed camera images, which are believed as zones of micro-cracks. Therefore, this point can be called 'micro-crack initiation'.

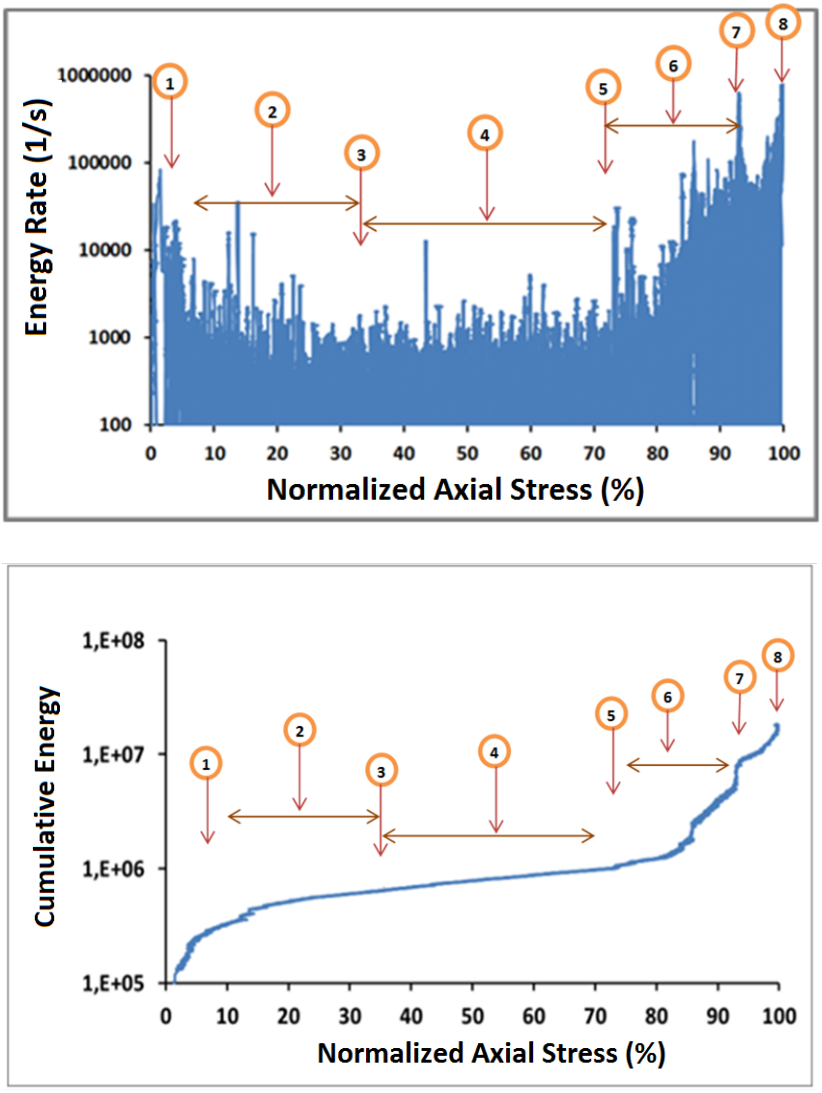

Figure 12: Plots of a) AE energy rate (per second) and b) cumulative AE energy versus the applied uniaxial stress normalized by the peak strength for the granite specimen AE-GR-2a-30-30. Numbers indicate cracking levels. Note that there is no significant difference between AE energy peaks before and after micro-crack initiation (level 3).

4.4.Micro-Crack Growth (Stable Crack Growth)

High speed camera images of the specimen after micro-crack initiation revealed that micro-cracks appear in the form of white patches and, for the most part, are isolated from one another. As micro-cracks increase, both in number and size, they eventually begin to interact with one another.

Level 4 in Figure 9 shows constant-magnitude peaks in the hits rate graph and a constant increase in the cumulative hits graph. On the other hand, level 4 in Figure 12 demonstrates that the energy of the AE signals in both the rate and cumulative graphs is almost constant and does not change a lot. This continual constant increase of AE activity after micro-crack initiation can be indicative of 'stable crack growth'.

4.5.Micro-Crack Coalescence (Macro-crack Initiation)

At 70-80% of the peak strength, the rate of the AE hits increases dramatically and the slope of the cumulative graph increases sharply (level 5 in Figure 9). This indicates the transition from a micro-cracking-dominated process to a process dominated by the propagation of a few large cracks, revealed by the occurrence of a high amount of AE energy (after level 5 in Figure 12). Other researchers (Eberhardt et al. 1998, Diederichs et al. 2004, Nicksiar and Martin 2012) have called this point 'crack damage'. With photographic monitoring of the granite specimen (Figure 11b), macro-cracks were detected at 74% peak strength which corresponds well to the results of AE detection. From high speed camera images, it can be seen that the initial macro-cracks are also produced near or at the tip of the flaws and parallel to the axial loading.

4.6.Macro-Crack Growth (Unstable Crack Growth)

As the load is increased, additional cracks begin to grow, incrementally contributing to the degradation of the inherent rock strength. This is evident in the AE data that show increasing bursts of AE activity (level 6 in Figures 9 and 12).

Previous studies have defined unstable crack propagation as the condition that occurs when the relationship between the applied stress and the crack length ceases to exist and other parameters, such as the crack growth velocity, take control of the propagation process. Under such conditions, crack growth continues even if the applied load is kept constant (Brace 1964, Bieniawski 1967a, Wawersik and Fairhurst. 1970).

4.7.Macro-Crack Coalescence

Macro-crack coalescence is defined as the point where macro-cracks connect. At this point a significant drop occurred in the amount of AE hits (level 7 in Figure 9a) and the rate of the cumulative hits plots inclines to zero (level 7 in Figure 9b). This phenomenon may partially happen during macro-crack growth (Level 6) but it happens mostly during macro-crack coalescence (Level 7). When the rate of cracking is high, two cracks in the rock may occur together so that the second hit from the second crack passes the threshold while the first hit is still being measured. This caused overlapping of the hits. This problem doesn't let the system to define the waveform based on HDT, instead based on max duration.

Another phenomenon that may cause overlapping of the hits is reflections of the signals. Close to the failure point, the reflections of the signals are strong enough to pass the threshold so that they overlap with the next coming hits within the HDT and therefore the system is again forced to define the hit not by HDT but by cutting it based on max duration. This drop in the number of

hits happened even after reducing the max duration as law as 3 ms, equal to the time length of the registered waveform (file length/sampling rate).
In these cases, the number of hits will decrease, because hits are overlapped instead of being detected individually. On the other hand, the duration, counts, energy and signal strength will be approximately the sum of those of the contributing signals. Blocking the traversing path of the AE signals by macro-cracks may also reduce the signal detection rate and causes a drop in the hits rate graph. It should be noted that though this overlapping behavior happens for brittle rocks however it may not be seen in non-brittle rocks. If loading rate is considerably low, this phenomenon may not happen either.

In order to have an idea about the time difference between macro-crack coalescence and failure, the AE hits and axial stress are plotted versus time for the granite specimen AE-GR-2a-30-30 in Figure 13. The results reveal that there is a time interval between the 'macro-crack coalescence' point and failure. This means that the specimen does not break right after the macro-crack coalescence.

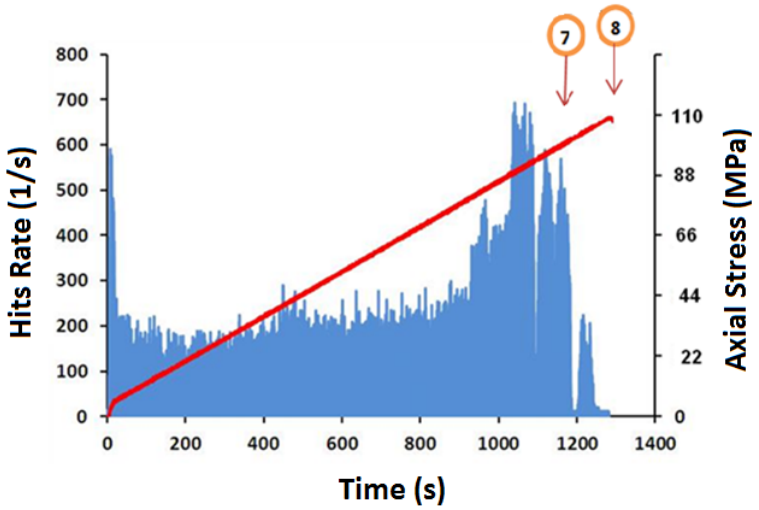

Figure 13: AE hits rate and axial stress versus time of the test for the granite specimen AE-GR-2a-30-30. The arrows and the numbers show that there is a time interval between macro-crack coalescence (level 7) and failure (level 8).

At this stage, macro-cracks propagate unstably in different directions to the axial loading (parallel and oblique) and finally coalesce (Figure 11c). Using photographic monitoring, macro-crack coalescence was detected at 92% peak strength, which corresponds well to the results of AE detection.

4.8.Failure

After coalescence of the macro-cracks the specimen does not yet fail. This is mostly caused by friction between the crack surfaces that are typically jagged in shape (saw-toothed) (Morgan et al. 2013). When the applied load overcomes both cohesion and friction of the grains adjacent to the crack surfaces, the specimen cannot resist any longer and falls apart (Figure 11d).

5. Discussion

Materials show zero AE activity or close to the background level as long as they remain below the largest previously experienced stress value. As this memorized stress is reached, the AE activity increases. This phenomenon is known as Kaiser Effect (Lavrov 2003). The Kaiser effect may mask the micro-crack initiation threshold of rocks (Diederichs et al, 2004). If crack initiation stress is lower than the previously experienced stress, because of the Kaiser Effect, the rock specimen does not show AE activity and the crack initiation point is shifted to a higher stress value. To show how Kaiser effect changes the micro crack initioation point, a granite specimen (AE-GR-a-45-60, Figure 14) that had been already loaded up to 60% of its peak strength was tested again but this time until it failed. Figure 15a shows AE hit rate vs normalized axial stress for the second loading. As Figure 15a, displays, the specimen did not show distinct AE activity in the 30-40 % peak strength that was considered as micro crack initiation point for the specimen AE-GR-2a-30-30 (Figure 9a), discussed in previous sections. Instead it showed the micro crack initiation at around 60% of peak strength due to Kaiser Effect. This phenomenon was confirmed after checking the high speed camera images of the specimen (Figure 16).

Figure 14: Photo of the AE-GR-a-45-60 specimen before and after the test

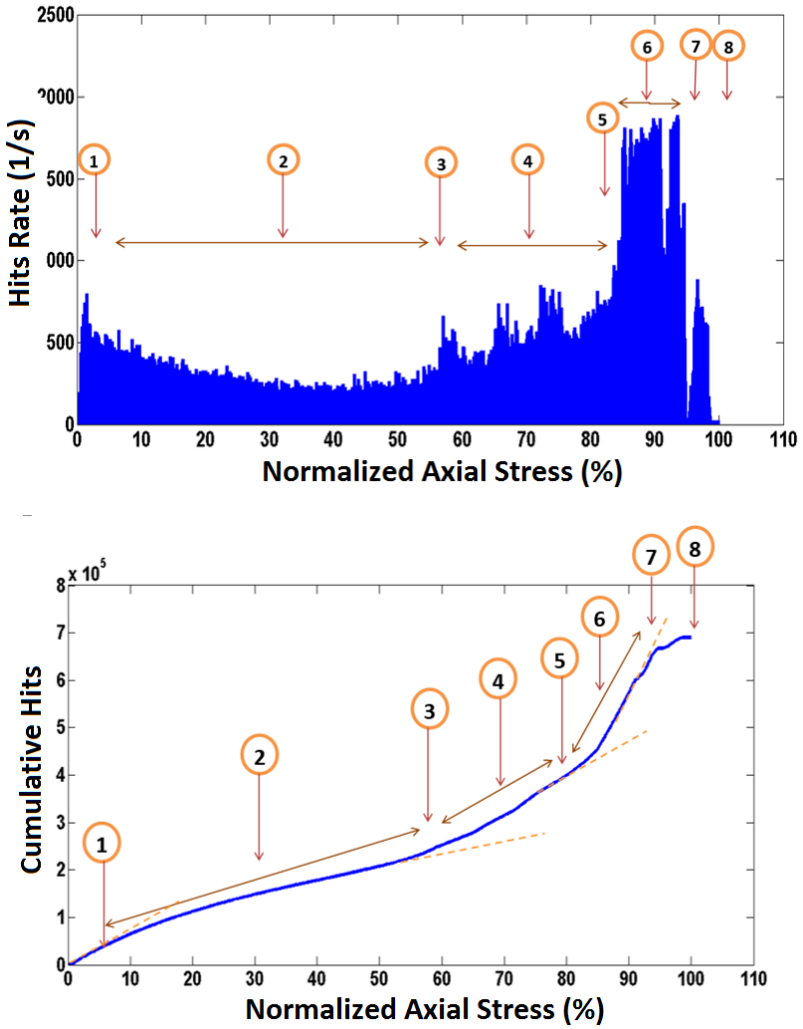

Figure 15: Plots of hits rate (per second) and cumulative hits versus the applied uniaxial stress normalized by the peak strength for the granite specimen AE-GR-a-45-60 for its second loading stage. Due to Kaiser Effect, the specimen shows micro-crack initiation at 60 % peak strength instead of 40 %. The numbers indicate cracking levels.

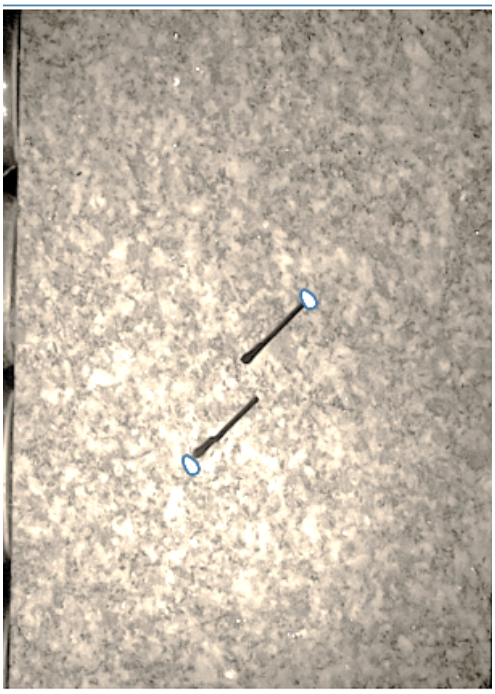

a: Micro-crack initiation (60% maximum loading, 82 MPa, 0.78 % axial strain). Micro-cracks show off as the form of white patches.

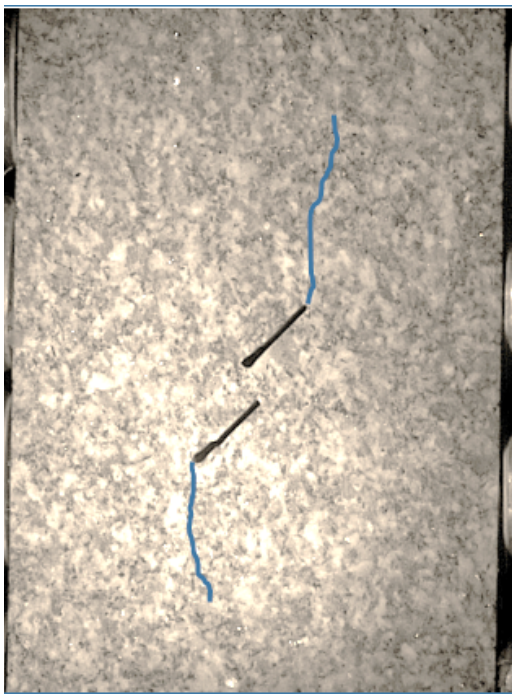

b: Macro-crack initiation (85% maximum loading, 102 MPa, 0.88 % axial strain).

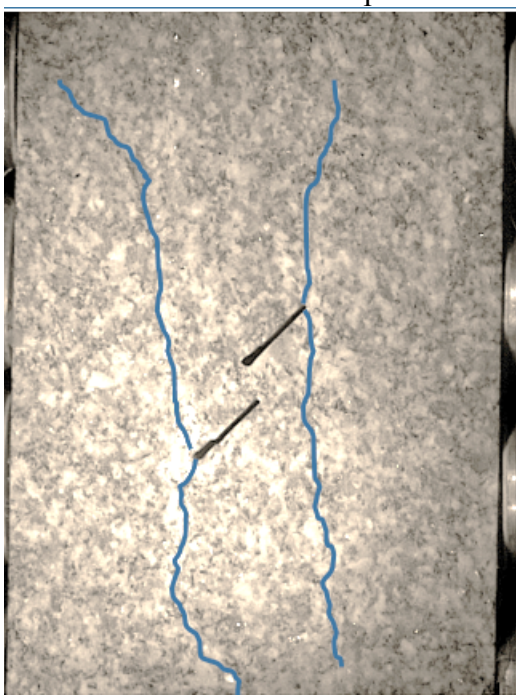

c: Macro-crack coalescence (95% maximum loading 113 MPa, 0.93 % axial strain).

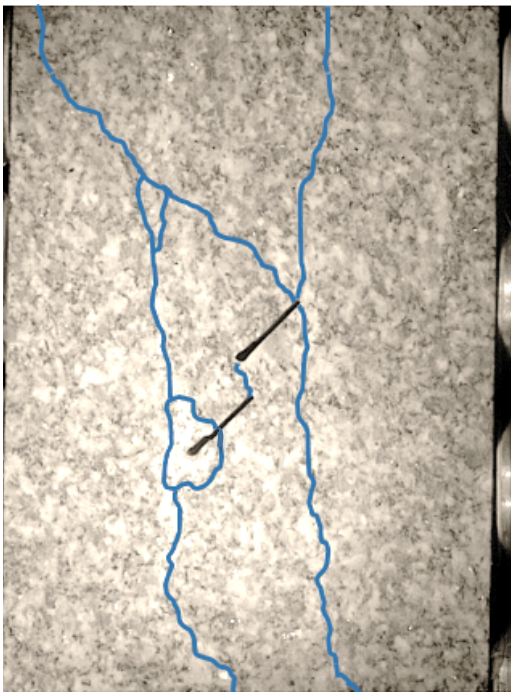

d: Failure (119 MPa, axial strain 0.98 %). Spalling occurred at the outer tip of the lower flaw.

Figure 16: High speed camera images of the granite specimen AE-GR-a-45-60 at different crackling levels

Figure 17 shows the rate and cumulative graphs of the AE energy for the granite specimen AE-GR-a-45-60. It can be seen that in the contrary to the first specimen (Figure 12), the second specimen shows an increase in the Energy rate and cumulative graphs right after micro-crack initiation (level 3). This indicates that rocks may start micro-cracking due to Kaiser Effect lately but if they start cracking, they generate signals with higher energies. In other words, due to Kaiser Effect, rocks preserve their cracking energy until they pass the previous experienced stress and then they release it faster than usual.

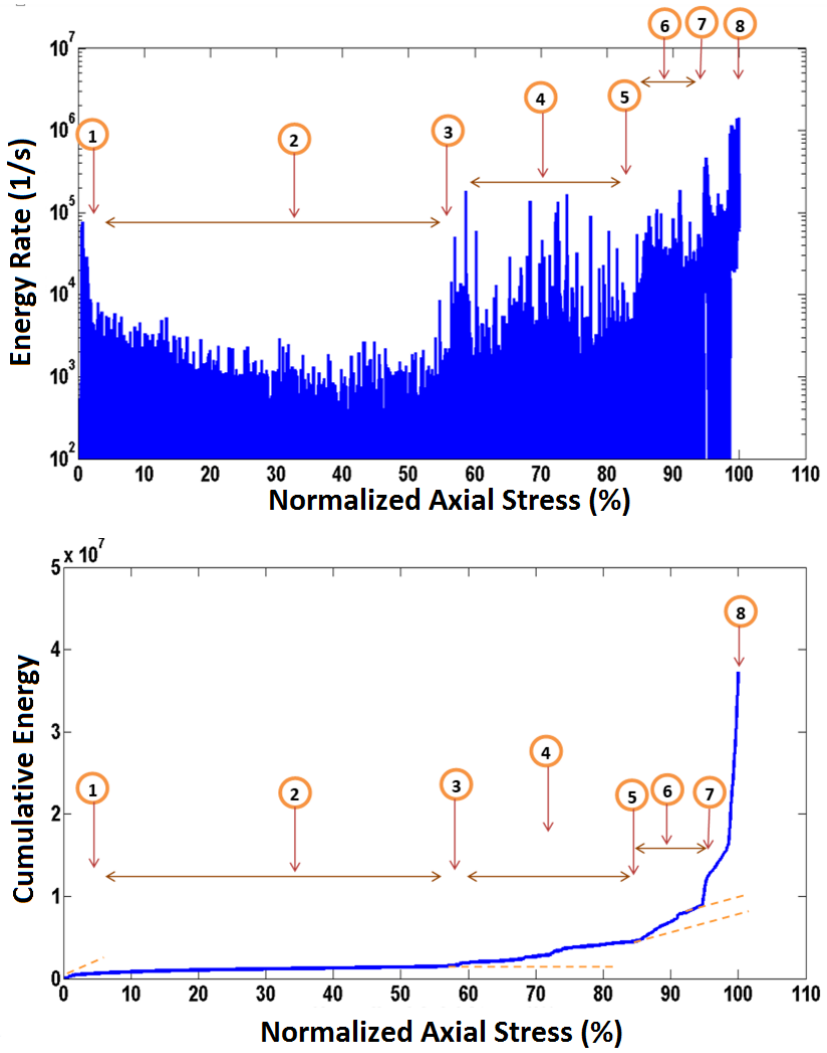

Figure 17: Plots of energy rate (per second) and cumulative energy versus the applied uniaxial stress normalized by the peak strength for the granite specimen AE-GR-a-45-60 for its second loading stage. Due to Kaiser Effect, the specimen shows micro-crack initiation at 60 % peak strength instead of 40 %. The numbers indicate cracking levels.

6. Conclusions

Cracking processes in granite were investigated with a combined analysis of AE parameters, photographic monitoring and stress-strain behavior. Based on the obtained results, the following conclusions can be reached:

- Eight different cracking levels have been identified in this paper. These are: 1) Crack closure, 2) linear elastic deformation, 3) micro-crack initiation (white patch initiation), 4) micro-crack growth (stable crack growth), 5) micro-crack coalescence (macro-crack initiation), 6) macro-crack growth (unstable crack growth), 7) macro-crack coalescence and 8) failure.
- Crack closure may or may not be present in the stress–strain response as it depends on the number of pre-existing cracks in the samples being tested. Nevertheless, some AE activity may occur because of specimen set up.
- AE signals show some activity during linear elastic deformation. This specific AE activity may be related to shear sliding of the pre-existing crack surfaces proposed by Bieniawski (1967b).
- Over several years, micro-crack initiation has been simply known as 'crack initiation' without any differentiation between micro- and macro-cracks. Combined use of acoustic emission and photographical monitoring revealed that this point is better described as 'micro-crack initiation'
- Coalescence of the micro-cracks produces macro-cracks. The macro-crack initiation is detected very well by a sharp increase in the AE parameters.
- It is believed that superimposition of the AE hits who come to the sensor together or in a very short time interval along with the reflections of the signals cause the system to define the hits based on max duration rather than HDT. It means that several hits may be registered as one single hit. Macro-cracks block the traversing path of the AE signals, and therefore signals on the other side of the crack may not be detected. These phenomena decrease the number of the hits in crack-coalescence point. As a result, AE hits show a drop at macro-crack coalescence and the slope of the cumulative hits graphs trends to zero.

Acknowledgement

The research was supported financially through a Collaborative Research and Development Grant from Natural Sciences and Engineering Research Council of Canada and Hydro-Quebec. The authors would also like to thank Université de Sherbrooke for providing the AE equipment.

References

1. Andersson C, Martin CD, Stille H (2009) The Äspö pillar stability experiment: part II—rock mass response to coupled excavation-induced and thermal-induced stresses. Int J Rock Mech Min Sci 46(5): 865–878
2. Bieniawski ZT (1967a) Mechanism of brittle fracture of rock, part I—theory of the fracture process. Int J Rock Mech Min Sci Geomech Abstr 4(4): 395–406
3. Bieniawski ZT (1967b) Mechanism of brittle fracture of rock, part II—experimental studies. Int J Rock Mech Min Sci Geomech Abstr 4(4): 407–423
4. Bobet A, Einstein HH (1998) Fracture coalescence in rock-type materials under uniaxial and biaxial compression. Int J Rock Mech Min Sci 35(7): 863–888
5. Brace, W.F. 1964. Brittle fracture of rocks. In State of Stress in the Earth's Crust. (ed Judd), 111-180. New York: American Elsevier Publishing Co.
6. Brace WF, Paulding B, Scholz C (1966) Dilatancy in the fracture of crystalline rocks. J Geophys Res 71:3939–3953
7. Brooks Z., F. -J. Ulm, H. H. Einstein. 2013. Environmental scanning electron microscopy (ESEM) and nanoindentation investigation of the crack tip process zone in marble. Acta Geotechnica, Volume 8, Issue 3, pp 223-245

8. Damjanac, B. and C. Fairhurst. 2010. Evidence for a long-term strength threshold in crystalline rock. Rock Mechanics and Rock Engineering, 43(5), 1-19.
9. Diederichs MS, Kaiser P, Eberhardt E (2004) Damage initiation and propagation in hard rock during tunneling and the influence of near-face stress rotation. Int J Rock Mech Min Sci 41(5): 785–812
10. Diederichs MS (2007) The 2003 Canadian Geotechnical Colloquium: mechanistic interpretation and practical application of damage and spalling prediction criteria for deep tunneling. Can Geotech J 44:1082–1116
11. Eberhardt E, Stead D, Stimpson B, Read R (1998) Identifying crack initiation and propagation thresholds in brittle rocks. Can Geotech J 35(2): 222–233
12. Goldsmith W, Sackman JL, Ewert C (1976) Static and dynamic fracture strength of Barre Granite. Int J Rock Mech Min Sci Geomech Abstr 13:303–309
13. Griffith, A. A., 1921. The phenomena of rupture and flow in solids. Phil. Trans. R. Soc. Lond. A, 221, 163-197.
14. Lajtai EZ (1974) Brittle fracture in compression. Int J FractMech 10:525–536
15. Lavrov, A., "The Kaiser effect in rocks: Principles and stress estimation techniques," International Journal of Rock Mechanics and Mining Sciences, Vol. 40, No. 2, pp. 151-171 (2003).
16. Lockner D. 1993. The role of acoustic emission in the study of rock fracture. Int J Rock Mech Min Sci Geomech Abstr 30:883–899
17. Martin CD, Chandler NA (1994) The progressive fracture of Lac du Bonnet granite. Int J Rock Mech Min Sci Geomech Abstr 31(6): 643–659
18. Martin CD, Christiansson R (2009). Estimating the potential for spalling around a deep nuclear waste repository in crystalline rock. Int J Rock Mech Min Sci 46:219–228
19. Miller JT (2008) Crack coalescence in granite. MSc Thesis, Massachusetts Institute of Technology
20. Miller JT, Einstein HH (2008) Crack coalescence tests on granite. In: The 42nd U.S. Rock mechanics symposium (USRMS), June 29–July 2, 2008, San Francisco
21. Morgan, S.P.; Johnson, C.A.; Einstein, H.H. 2013. Cracking processes in Barre granite: fracture process zones and crack coalescence. International Journal of Fracture, v 180, n 2, p 177-204
22. Nicksiar, Mohsen, Martin, C.D. 2012. Evaluation of methods for determining crack initiation in compression tests on low-porosity rocks. Rock Mechanics and Rock Engineering, v 45, n 4, p 607-617
23. Nicksiar, Mohsen, Martin, C.D. 2014. Factors Affecting Crack Initiation in Low Porosity Crystalline Rocks. Rock Mechanics and Rock Engineering, p 1-17
24. Rojat F, Labiouse V, Kaiser PK, Descoeudres F (2009) Brittle rock failure in Steg Lateral Adit of the Lötschberg Base Tunnel. Rock Mech Rock Eng 42:341–359
25. Seto M.,Nag D.K., Vutukuri V.S. 1999. In-situ rock stress measurement from rock cores using the acoustic emission method and deformation rate analysis. Geotechnical & Geological Engineering , Vol. 17, Issue 3-4, pp 241-266
26. Stacey TR (1981) A simple extension strain criterion for fracture of brittle rock. Int J Rock Mech Min Sci Geomech Abstr 18:469–474
27. Waversik, W.R and C. Fairhurst. 1970. A study of brittle rock fracture in laboratory compression experiments. Int. J. Rock Mech. Min. Sci., 7, 561-575.
28. Wong LNY, Einstein HH (2009) Crack coalescence in molded gypsum and Carrara marble: part 1-macroscopic observations and interpretation. Rock Mech Rock Eng 42(3): 475–511

29. Wong LNY, Einstein HH (2009) Crack coalescence in molded gypsum and carrara marble: Part 2-microscopic observations and interpretation. Rock Mech Rock Eng 42(3): 513–545
30. Xia K, Nasseri M.H.B, Mohanty B, Lu F, Chen R, Luo S.N, 2008. Effects of microstructures on dynamic compression of Barre granite. International Journal of Rock Mechanics & Mining Sciences 45: 879–887